ACS APPLIED MATERIALS & INTERFACES

Research Article

www.acsami.org

Forming-Free Resistive Switching in Multiferroic $BiFeO_3$ thin Films with Enhanced Nanoscale Shunts

Xin Ou,*[,†] Yao Shuai,*[,‡] Wenbo Luo,[‡] Pablo F. Siles,[§,#] Reinhard Kögler,[†] Jan Fiedler,[†] Helfried Reuther,[†] Shengqiang Zhou,[†] René Hübner,[†] Stefan Facsko,[†] Manfred Helm,[†] Thomas Mikolajick,[⊥] Oliver G. Schmidt,[§,#] and Heidemarie Schmidt*[,§]

[†]Institute of Ion Beam Physics and Materials Research, Helmholtz-Zentrum Dresden-Rossendorf (HZDR) e.V., P.O. Box 510119, 01314 Dresden, Germany

[‡]State Key Laboratory of Electronic Thin Films and Integrated Devices, University of Electronic Science and Technology of China, Chengdu 610054, China

[§]Material Systems for Nanoelectronics, Technische Universität Chemnitz, Reichenhainerstraße 70, 09107 Chemnitz, Germany

[⊥]Institute of Semiconductors and Microsystems, Technische Universität Dresden and Namlab GmbHNöthnitzer Strasse 64, 01187 Dresden, Germany

[#]Institute for Integrative Nanosciences, IFW Dresden, Helmholtzstraße 20, 01069 Dresden, Germany

Supporting Information

ABSTRACT: A controlled shunting of polycrystalline oxide thin films on the nanometer length scale opens the door to significantly modify their transport properties. In this paper, the low energy Ar^+ irradiation induced shunting effect of forming-free, non-volatile resistive switching in polycrystalline $BiFeO_3$ thin film capacitor-like structures with macroscopic bottom and top contacts was investigated. Oxygen atoms at the $BiFeO_3$ surface are preferentially sputtered by Ar^+ ion irradiation and oxygen vacancies and a metallic Bi phase are formed at the surface of the $BiFeO_3$ thin film before deposition of the top contacts. A phenomenological model is that of nanoscale shunt resistors formed in parallel to the actual $BiFeO_3$ thin film capacitor-like structure. This model fits the noticeable increase of the retention stability and current density after irradiation. The formation of stable and conductive shunts is further evidenced by conductive atomic force microscopy measurements.

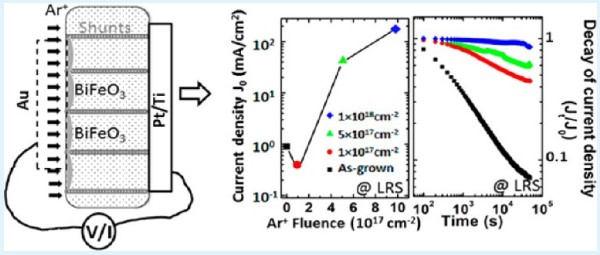

KEYWORDS: *resistive switching, Ar irradiation, shunting, oxygen vacancy, current retention, $BiFeO_3$*

1. INTRODUCTION

Optimization of electrical properties of many oxides strongly relies on tailoring oxygen vacancies (V_O) because of their important role in the formation of electrically active bulk and interface defects.[1] Recently, resistive switching (RS) of functional oxide thin films has attracted tremendous interest due to its promising application in high speed and high density nonvolatile memory devices.[2,3] By applying voltage pulses between metallic contacts on the oxide thin films, such functional oxide films are switched between different resistance states and may store information. This is the basis of resistive random access memory (RRAM) devices. The resistive switching phenomenon has been found in many metal oxides, which are mainly classified as ternary oxides[4−8] and binary metal oxides.[9−11] Two models, the interface-type model and filamentary conducting model, have been proposed as the possible driving mechanism for RS.[2] The characteristics of RS oxides are strongly influenced by the amount and distribution of oxygen vacancies and the valence of metallic elements.[2] An approach to tune the transport properties in RS oxides is the formation of oxygen vacancies, V_O. The creation of V_O in RS oxides can be referred to as a "defect doping" process. Furthermore, several works demonstrated that low-energy Ar^+ ($\leqslant$1 keV) irradiation is an efficient tool to create oxygen vacancies in the surface layer of bulk $SrTiO_3$ substrate, and enhanced electrical conductivity,[12−14] blue-light emission,[15] and anisotropic magnetotransport[16,17] are observed in Ar^+ irradiated $SrTiO_3$.

$BiFeO_3$ has the same perovskite structure as $SrTiO_3$ and is one of the most intensively investigated multiferroic materials because of its potential for coupling the electric and magnetic orders.[18] $BiFeO_3$ has received great attention also due to its high ferroelectric Curie temperature ($T_C \sim 1103$ K) and antiferromagnetic Néel temperature ($T_N \sim 640$ K).[19] In addition to the impurity doping process, low-energy Ar^+ irradiation is promising for realizing the electrical or magnetic

Received: September 24, 2013
Accepted: November 8, 2013
Published: November 8, 2013

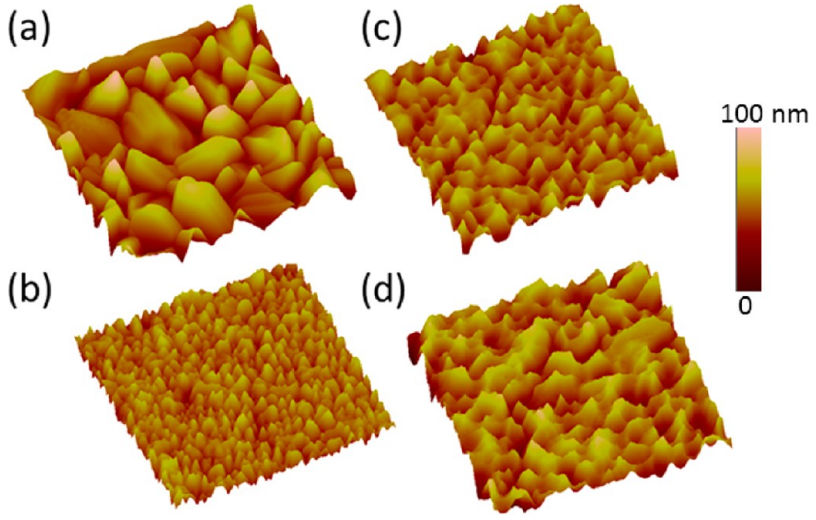

Figure 1. Three-dimensional AFM images of (a) the as-grown $BiFeO_3$ films and (b–d) $BiFeO_3$ films irradiated by 300 eV Ar^+ ions with a fluence of (b) 1×10^{17} cm^{-2}, (c) 5×10^{17} cm^{-2}, and (d) 1×10^{18} cm^{-2}. The scanning size is 4×4 μm^2. The AFM color scale (right) represents the height information.

modulation of the $BiFeO_3$. The investigation of irradiation effects in $BiFeO_3$ is of physical and technological importance. Very recently, the RS effects have been observed in undoped and doped $BiFeO_3$ by different groups.[5,20−24] An Au/$BiFeO_3$/Pt capacitor-like structure shows a bistable interface-related resistive switching that needs no pre-electroforming step.[5] This type of RS results from the change of Schottky barrier formed at the interface of metallic contact/perovskite oxide under the applied voltage.[25] However, interface-related resistive switching typically suffers from insufficient read current and unstable resistive switching states.[2,5,27] Both are critical issues for a reliable circuit operation in memory cells and other devices fabricated using the crossbar architecture, e.g., in neuromorphic circuits.[28] Sufficient and stable read current are also critical for the applicability of $BiFeO_3$ based devices.

In this paper, we investigated the stoichiometry and nanostructure changes in $BiFeO_3$ films on Pt bottom electrodes induced by Ar^+ irradiation. A controllable formation of V_O and Bi metallic phase is found in the near-surface region of Ar^+ irradiated $BiFeO_3$, resulting in a noticeable increase of the current density and a significant improvement of retention stability of Au/$BiFeO_3$/Pt capacitor-like structures. The experimental results are discussed based on engineering of the Schottky contact in combination with the formation of stable and conductive shunts. We visualize the formation of nanoscale shunts by conductive atomic force microscopy (C-AFM) measurements and introduce a phenomenological model that fits the noticeable increase of the retention stability and current density after irradiation.

2. EXPERIMENTAL SECTION

500 nm thick $BiFeO_3$ films were deposited on Pt/Ti/SiO_2/ Si substrates at 650 °C using pulsed laser deposition. As-grown $BiFeO_3$ films were irradiated by Ar^+ ions with a series of ion energies and fluences. The low-energy Ar^+ beam is generated via a Kaufman ion source in a high vacuum chamber with a base pressure of 10^{-8} mbar. During the Ar^+ irradiation the chamber is backfilled with Ar from the ion source to a pressure of 2.4×10^{-4} mbar. The surface temperature of the $BiFeO_3$ layer is around 250 °C monitored by an external infrared pyrometer. The thickness of $BiFeO_3$ (500 nm) is reduced during irradiation by sputtering. The thickness reduction amounts to 99 nm and 143 nm for an applied Ar^+ fluence of 5×10^{17} cm^{-2} and 1×10^{18} cm^{-2}, respectively, as confirmed by surface profilometry measurements using a Dektak8 from Veeco. Some of the samples were post-annealed at 500 °C for 30 min in a pure Ar atmosphere or in a 5% oxygen containing atmosphere. After irradiation, the Au top electrode with a size of 100 $\mu m \times 300$ μm was deposited by magnetron sputtering onto the $BiFeO_3$ films through a shadow mask. A scheme of the Au/$BiFeO_3$/ Pt capacitor-like structure is displayed in the inset of Figure 5a. The concentration ratio of Bi, Fe and O at the $BiFeO_3$ surface as a function of the Ar^+ fluence was simulated by the TRIDYN code.[29] The surface morphology of the samples was characterized by a multi-mode AFM system. X-ray photoelectron spectroscopy (XPS) measurements were performed with a scanning Auger electron spectrometer Microlab 310F. Cross-sectional transmission electron microscopy (XTEM) was performed with an image-corrected FEI Titan 80-300 microscope. The electrical measurements were carried out using a Keithley 2400 source meter and via local current sensing AFM techniques (C-AFM) with an Agilent Series 5500 AFM system. A scheme of the C-AFM measurement is shown in Figure 4a.

3. RESULTS AND DISCUSSION

A. Defect Formation in $BiFeO_3$ due to Ar^+ Irradiation.

The preferential sputtering of the $BiFeO_3$ film and dynamic composition changes under Ar^+ irradiation have been simulated by using the TRIDYN code (see the Supporting Information).[29] The results show that the ratio of oxygen atoms to iron/bismuth atoms is significantly reduced under the Ar^+ fluences used in this experiment. As the oxygen atoms are preferentially removed from their sites, oxygen vacancies are continuously produced during the irradiation. Once the V_O are created in the penetration depth of the Ar^+ ions (6.5 nm), they may diffuse into the bulk of the $BiFeO_3$ film driven by concentration gradient of V_O under irradiation at elevated temperature.[30] The irradiation effect on the surface morphology of $BiFeO_3$ films by Ar^+ irradiation with different fluences was investigated by AFM and is shown in Figure 1. The as-grown $BiFeO_3$ film surface consists of randomly oriented grains with a typical size of 300 nm. After Ar^+ irradiation at a small fluence of 1×10^{17} cm^{-2}, the surface grains become smaller and more uniformly orientated. The surface grain size is reduced to around 100 nm and the surface is smoother. The surface roughness is reduced from 21 to 15 nm. As the Ar^+ fluence is increased to 5×10^{17} cm^{-2} and 1×10^{18} cm^{-2}, the size of

surface grains increases again and a number of prolonged cracks appear on the surface. This is in agreement with our observation from the scanning electron microscopy. Similar behavior has also been observed on ion-irradiated polycrystalline metal films.[31]

In principle, the creation of $V_O^{\cdot}$ is accompanied by the change of the valence of metallic elements in the oxide. The chemical states of Bi at the surface were investigated by XPS. Figure 2a shows the XPS spectra of Bi-4f peaks. The spectrum of the as-grown sample consists of two peaks at 159.5 eV (peak A) and 164.8 eV (peak B). This matches well with the spin orbit splitting energy of 5.36 eV in Bi-4f related to oxide states of Bi (Bi_{ox}). In contrast, the irradiated sample spectrum consists of four peaks with two additional sub-peaks at 157.4 eV (peak C) and 162.7 eV (peak D). The presence of these two sub-peaks is associated with a metallic Bi phase (Bi_m),[32,33] which forms because of the broken Bi−O bonds generated by preferential sputtering of O under the energetic Ar^+ ion irradiation. The integrated area of total Bi peaks (A + B + C + D) of the irradiated sample is smaller than that of the as-grown sample (A + B). However, the ratio of the integrated area of the Bi peaks C and A, and the ratio of the Bi peaks D and B increases with increasing fluence (Figure 2b). This indicates that the valence of Bi continuously changes from covalent (Bi peaks A and B) to metallic (Bi peaks C and D) during the irradiation.

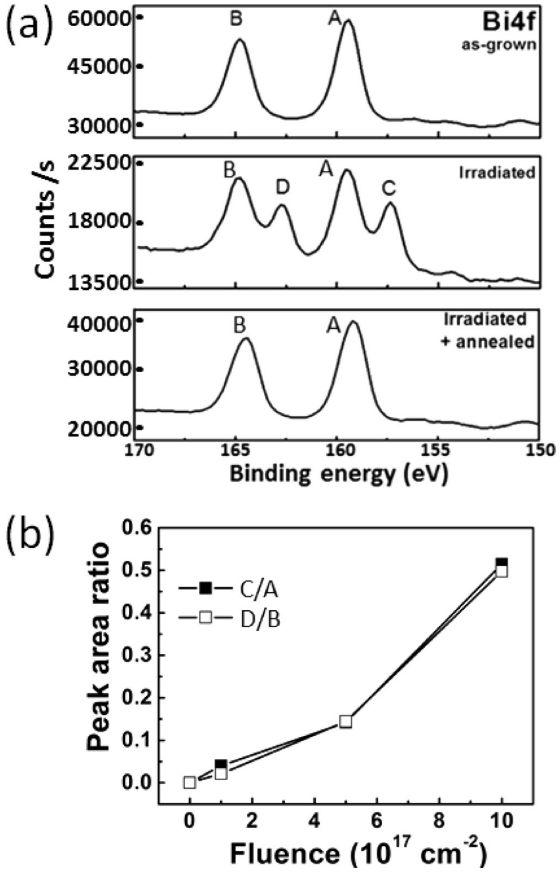

Figure 2. (a) XPS spectra for Bi 4f of $BiFeO_3$ as-grown, irradiated with a 300 eV Ar^+ beam with a fluence of 1×10^{18} cm^{-2} and irradiated plus post-annealed at 500 °C for 30 min (independent of annealing atmosphere). The Bi 4f peaks located at 159.5 and 164.8 eV, (main peaks) and at 157.4 and 162.7 eV (sub-peaks) are marked as A, B, C, and D, respectively. (b) The ratio of the integrated area of the Bi peaks C and A, and the ratio of the integrated area of the Bi peaks D and B in dependence on the Ar^+ fluence.

During the $BiFeO_3$ deposition, different types of defects, such as dislocations, grain boundaries, ions, and oxygen vacancies are created. Images a and b in Figure 3 show bright-field XTEM images of the as-grown and irradiated polycrystalline $BiFeO_3$ films. Some of the defects, e.g., grain boundaries, are randomly distributed and orientated. Other grain boundaries are more aligned and passing through the entire layer of the $BiFeO_3$ film. These defects may trap (charged) V_O and form conductive channels inside the $BiFeO_3$ film. In contrast to the volume of $BiFeO_3$ grains, the irradiated surface layer with a thickness of 6.5 nm shows nanocrystals embedded in an amorphous matrix (Figure 3c). The nanocrystals may be formed by different Bi phases (Bi_{ox} and Bi_m) in the composite after the collision with Ar^+ ions. Images d and e in Figure 3 show high-angle annular dark-field scanning TEM (HAADF-STEM) images of the near surface region of as-grown and irradiated $BiFeO_3$ films. In contrast to the virgin surface, a darker surface layer is visible in the irradiated $BiFeO_3$ film, which indicates a deficiency of heavy elements, e.g., deficiency of Bi, in this layer. This is confirmed by energy-dispersive X-ray spectroscopy (not shown) and is in agreement with the XPS results shown in Figure 2a. We ascribe the reduction of the total Bi (Bi_{total}) content in the irradiated surface layer to a

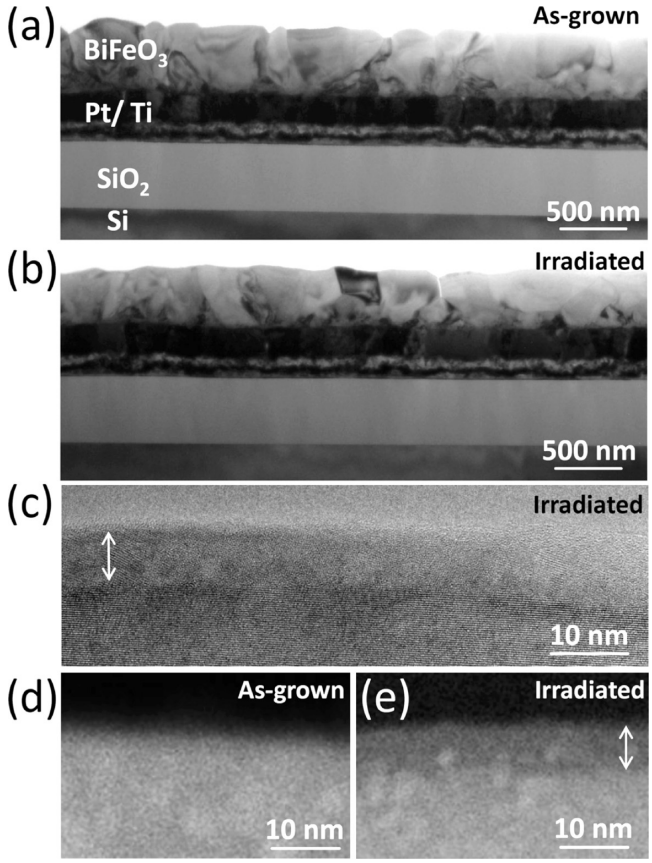

Figure 3. Bright-field XTEM images of $BiFeO_3$/ Pt/Ti structure (a) as-grown and (b) irradiated with a 300 eV Ar^+ beam and a fluence of $1{\times}10^{18}$ cm^{-2}. (c) High-resolution XTEM image focusing on the cross-section of irradiated $BiFeO_3$. HAADF-STEM images of (d) as-grown and (e) irradiated samples. Arrows in (c) and (e) indicate the thickness of the modified surface layer in the irradiated $BiFeO_3$ film.

thermodynamical effect instead of collisions and ballistic transport effect simulated by TRIDYN code.[29] Bi is known to be highly volatile. Thus decomposition of Bi−O into Bi_m and O_2 enhances the evaporation of Bi from the surface during Ar^+ irradiation.[33,34] Nevertheless, according to Figure 2b, the ratio of Bi_m/Bi_{ox} in irradiated $BiFeO_3$ surfaces is relatively high (ca. 55%).

B. Transport Behavior in Irradiated $BiFeO_3$ on the Nanoscale. Conductive shunts can form in the local region of the V_O decorated grain boundaries with high density of gap states. Actually, this is evidenced by conductive AFM measurements shown in Figure 4 which give a direct visualization of the current variations on the $BiFeO_3$ surface. Comparing the topography (Figure 4b) and current image (Figure 4c), it is shown that the current preferentially goes through the irradiated $BiFeO_3$ film along the grain boundaries or cracks around the $BiFeO_3$ grains. This has not been observed in the as-grown sample due to the very low current signals along the grain boundaries. These conductive channels based on V_O decorated grain boundaries or cracks may serve as short-circuits (shunts) between the Au and Pt electrode in a device structure.

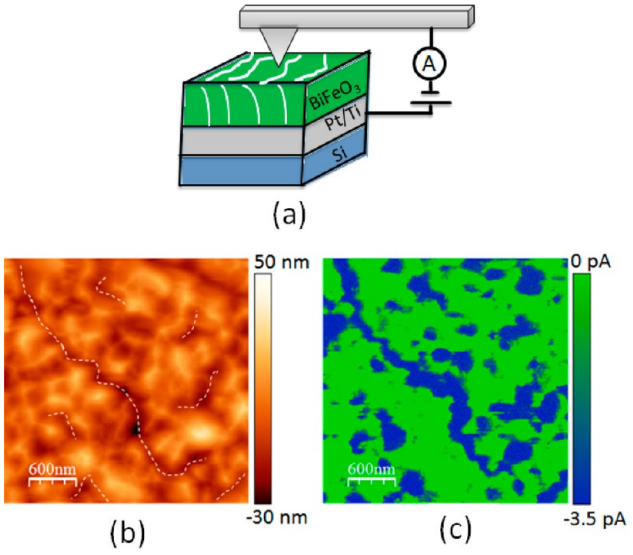

Figure 4. (a) Schematic of the conductive AFM measurement on $BiFeO_3$/Pt/Ti/Si. A grounded conductive Pt-coated tip and a Pt layer under the $BiFeO_3$ film serve as the front and bottom contact, respectively. The voltage (−9 V) is applied from the back contact ($BiFeO_3$/ Pt). The voltage polarity is opposite to the $I-V$ measurements shown in Figure 5. The white stripes mark the conductive shunts which are formed in the irradiated $BiFeO_3$ layer. Conductive AFM images of the $BiFeO_3$ films irradiated by 300 eV Ar^+ ions with a fluence of 1×10^{18} cm^{-2}, (b) topography image, (c) current image. The dashed lines shown in (b) serve as guides to the eye for grain boundaries or cracks. The negative current shown in (c) is due to the polarity of the applied voltage.

C. Forming-Free Resistive Switching Enhanced by Nanoscale Shunting. Current−voltage (I−V) characteristics of Au/$BiFeO_3$/ Pt capacitor-like device structures with and without Ar^+ irradiation are shown in Figure 5. In both cases the $I-V$ curves were taken for a voltage varying in different bias ranges from ±4.0 V in steps of 0.5 V to ±6.5 V. The curves show the $I-V$ characteristics which are asymmetric in the positive and negative voltage range. This is attributed to the

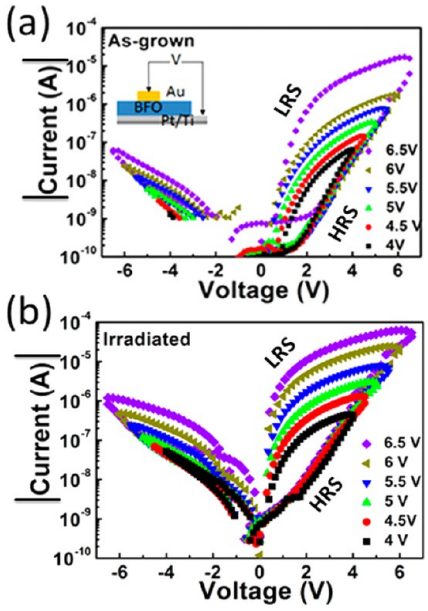

Figure 5. $I-V$ characteristics of a Au/$BiFeO_3$/Pt capacitor-like structure with (a) as-grown and (b) irradiated by 300 eV Ar^+ ions for 15 min with a fluence of 5×10^{17} cm^{-2}. Note that the detection limit is 1×10^{-9} A in negative bias mode.

asymmetric electrical contact barriers in the Au/$BiFeO_3$/ Pt structure. The more pronounced $I-V$ hysteresis appears in the positive voltage range with two different resistance states for each applied voltage. The positive voltage range will be the reading range of a RS device. During the voltage ramp in positive direction, the $I-V$ curves represent the high resistance states (HRS). Their path is nearly the same, independent of the maximum voltage. However, the $I-V$ curves during the voltage ramp in negative direction are well separated from each other. They represent different low resistance states (LRS) depending on the applied maximum voltage. Such multi LRS behavior offers an opportunity for designing a multilevel RS device, which is based on the Au/$BiFeO_3$/ Pt capacitor-like structure.[35] For Ar^+ irradiation with an ion energy of 300 eV and an ion fluence of 5×10^{17} cm^{-2}, the resulting $I-V$ curves in Figure 5b shift upward by about one order of magnitude as compared to the $I-V$ curves of the as-grown material and their separation at LRS is more uniform. These two aspects of the improved device characteristics are further demonstrated in Figure 6 by a retention test for irradiation with different Ar^+ fluences and energies. Figure 6a shows the current density (J) measured by giving 500 voltage pulses of +2 V (reading pulse, U_r) to the samples in LRS or in HRS within an interval of 100 s. There is a significant decay of the current density of the as-grown sample with increasing number of voltage pulses. This decay is more pronounced in LRS than in HRS. Figure 6b shows that the decay of the normalized current density in LRS is significantly suppressed via Ar^+ irradiation, i.e., the retention behavior is improved with increasing irradiation fluence. This improvement is confirmed by the retention measurement performed both at room temperature and at an elevated temperature of 385 K. Figure 6c shows that the current density at LRS increases as the Ar^+ fluence increases beyond 1×10^{17} cm^{-2}, and a current density two orders of magnitude higher than for the as-grown sample was achieved by Ar^+ irradiation with a fluence of 1×10^{18} cm^{-2}. The retention behavior is quantitatively compared by the ratio of the last and the first measured current density

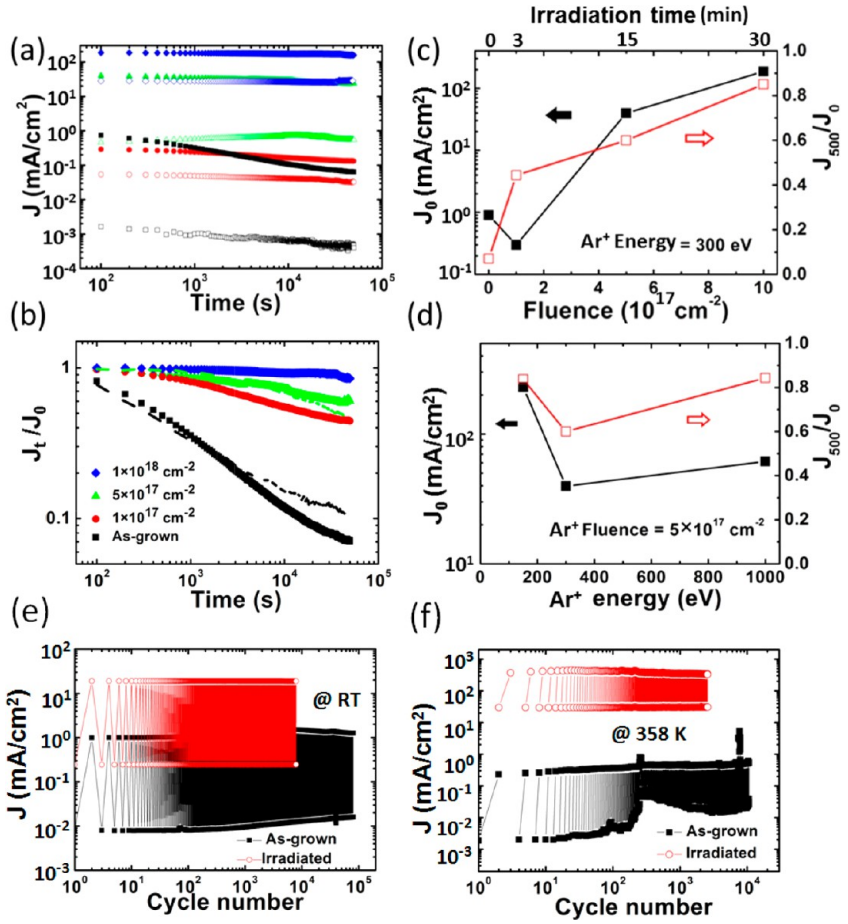

Figure 6. (a) Retention characteristics of the current density (J) of the Au/$BiFeO_3$/Pt structure for 500 pulses of a read voltage of +2 V with a repetition frequency of 100 s. The pulse length is 100 ms. The $BiFeO_3$ films are either as-grown (black squares) or irradiated by 300 eV Ar^+ ions with a fluence of 1×10^{17} cm^{-2} (red circles), 5×10^{17} cm^{-2} (green triangles), and 1×10^{18} cm^{-2} (blue diamonds). Solid and hollow symbols show the current density at LRS and HRS, respectively. (b) Normalized current density at LRS vs. retention time. The current density values taken at different time (J_t) are normalized by the initially measured current density value (J_0). The dashed curves indicate the retention measurement performed at the temperature of 385 K for sample as-grown (black) and irradiated (green) with a fluence of 5×10^{17} cm^{-2}. (c) The Ar^+ fluence and (d) energy dependence of the initially measured current density (J_0) at LRS (black solid squares, left scale) and of the ratio of the last and the first measured current value (J_{500}/J_0) during the retention test (red hollow squares, right scale). Endurance test at (e) room temperature and (f) 385 K of the as-grown (black solid squares) and irradiated (red hollow circles) Au/$BiFeO_3$/Pt capacitor-like structure with a device size of 100×300 μm^2. The Ar^+ fluence is (e) 5×10^{17} cm^{-2} and (f) 1×10^{18} cm^{-2}.The currents are taken at a read voltage of 1.66 V. The switching voltage is 7 V.

(J_{500}/J_0). As the Ar^+ fluence increases to 1×10^{18} cm^{-2}, the current density (J_{500}) after 5×10^4 s remains 85% of the first measured value (J_0), which is remarkably higher than that of the as-grown sample of 7%. The significant improvement of the retention behavior for the irradiated $BiFeO_3$ overcompensates the disadvantage of the reduced ON/OFF current ratio. In addition, stable and constant current levels at LRS and HRS are also demonstrated in the endurance test of the irradiated device with 1×10^4 and 3×10^3 write/erase cycles measured at room temperature (Figure 6e) and 385 K (Figure 6f), respectively. These improved characteristics allow a reliable device operation. Figure 6d indicates a minor effect of the increase of Ar^+ energy, whereas the increase of the Ar^+ fluence significantly enhances the current density.

The fluence dependence of the ratio between XPS peak area of metallic Bi_m and XPS peak area of oxidized Bi_{ox} shown in Figure 2b is in qualitative agreement with the increase of current density shown in Figure 6c. This is also confirmed by post-annealing effect of irradiated $BiFeO_3$ films. The Bi_m XPS peaks C and D vanish after post-annealing (Figure 2a) at 500 °C for 30 min, which is accompanied by a re-oxidation of Bi_m at the surface and the corresponding reduction of the current density. Figure 7 compares the initial current density value (J_0) at LRS and its retention time stability for as-grown, irradiated and irradiated plus post-annealed $BiFeO_3$ films. Post-annealing was performed in two different atmospheres: A1 (pure Ar) and A2 (with 5% O_2). In both cases, A1 and A2, Bi_m peaks in XPS spectra have disappeared (Figure 2a), J_0 is reduced to a value close to the original current level in the as-grown $BiFeO_3$ sample (Fig. 7a). In the case of the oxygen-containing atmosphere, J_0 is even below this level. However, the retention stability of the current density of the post-annealed $BiFeO_3$ sample dramatically depends on the oxygen content in the atmosphere. Figure 7b demonstrates that after post-annealing in pure Ar gas, the irradiated $BiFeO_3$ sample still keeps its improved retention stability. By post-annealing in oxygen containing ambient, the retention is deteriorated to the original behavior in the as-grown $BiFeO_3$ sample. This finding again underlines the important role of Bi_m and V_O for the increase in the current density and of the irradiation-induced V_O for improved retention behavior of Au/$BiFeO_3$/Pt capacitor-like structures. Note that the thickness reduction of the $BiFeO_3$

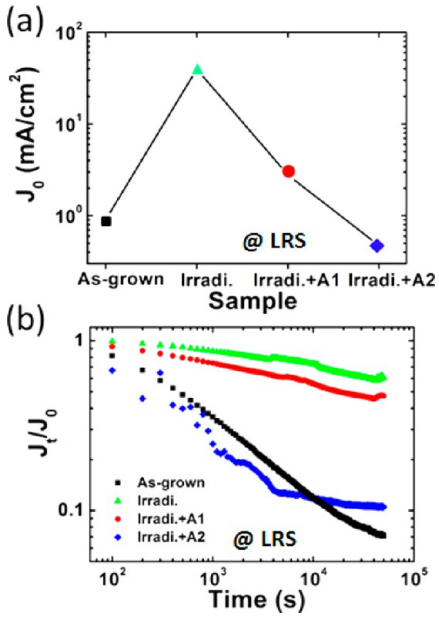

Figure 7. (a) Initially measured current density (J_0) at LRS in retention measurement for a $BiFeO_3$ film as-grown (black square), for a $BiFeO_3$ film irradiated (green triangle) with Ar^+ fluence of 5×10^{17} cm^{-2} and for a $BiFeO_3$ film irradiated plus post-annealed in different atmospheres of 100% Ar (A1, red circle) and of 95% Ar + 5% O_2 (A2, blue diamond). (b) Normalized current density at LRS vs. retention time. The current density values taken at different time (J_t) in the retention measurement are normalized by the initially measured current density value (J_0).

under irradiation is not important for the observed increase of the current density, because the irradiated plus post-annealed samples are thinner as well. To further confirm this point, we prepared a sample with 750 nm $BiFeO_3$, and the thickness reduction induced by Ar^+ irradiation is overcompensated by the thicker film. The increase of the current density and improved current retention is still observed in the Ar^+ irradiated sample with a thicker $BiFeO_3$ film.

D. Phenomenological Shunt Model. The irradiation-induced composition and structure deviation at the surface, i.e. the deficiency of Bi and O and the corresponding formation of V_O and the relative accumulation of a Bi_m phase, causes a reduction of the Schottky barrier at the interface between Au-contact and $BiFeO_3$ grains which is responsible for the nonvolatile RS effect. The formation of the Bi_m phase at the surface of $BiFeO_3$ grains may locally reduce the Schottky barrier height of Au/$BiFeO_3$ because of the lower work function of metallic Bi (4.31 eV). Furthermore, V_O are effective donors for n-type $BiFeO_3$. A higher concentration of V_O at the surface because of irradiation induces band bending and reduces the width of the depletion region. Both effects lead to an increase of the thermal emission and of the tunneling probability of electrons and contribute to the enhancement of the current density.[25,26]

To further elucidate the Ar^+ irradiation effect on the improvement of the RS characteristics, here we introduce a phenomenological model to explain the noticeable increase of the retention stability and current density after irradiation. This model describes a shunt resistor in parallel to the irradiated $BiFeO_3$ thin film capacitor-like structure. For a non-irradiated $BiFeO_3$ thin film capacitor-like structure the influence of the shunt resistor can be neglected and its total resistance can be described as a series of resistances

$$R_{BFO} = R_{Au/BiFeO_3} + R_{BiFeO_3} + R_{BiFeO_3/Pt} \quad (1)$$

where $R_{Au/BiFeO_3}$ and $R_{BiFeO_3/Pt}$ are junction resistances of the top (Schottky) and bottom contact, R_{BiFeO_3} is the bulk resistance of the non-irradiated $BiFeO_3$ thin film. When a positive voltage is applied, the Au/$BiFeO_3$ Schottky contact is biased in forward direction as $BiFeO_3$ is an n-type material. Under a negative switching pulse the Schottky contact at the Au/$BiFeO_3$ interface is in reversed direction and R_{BFO} is dominated by $R_{Au/BiFeO_3}$, which induces a low leakage current (Figure 5a). Contrary, the $BiFeO_3$/ Pt bottom contact is an Ohmic like contact according to the high current observed under positive voltages (Figure 5a). The low barrier height formed at the $BiFeO_3$/ Pt interface results from the inter-diffusion of Ti to this interface during the film deposition process at 650°C.[36] For the Au/irradiated $BiFeO_3$/ Pt capacitor, the $I-V$ curves show no appearance of electro-forming (Figure 5b). Instead, they show a dependence of LRS and HRS on the area of the Au top contact size (inset in Figure 8). This dependence may partially be caused by the increased

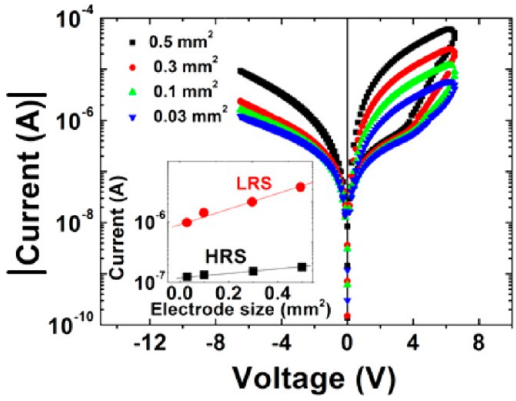

Figure 8. $I-V$ curves of Au/irradiated $BiFeO_3$/ Pt capacitor-like structure with different Au electrode sizes. The Ar^+ irradiation has been performed at 300 eV with a fluence of 5×10^{17} cm^{-2}. The inset shows that the current measured at a reading voltage of 2 V has a linear relationship with electrode size.

amount of conductive nanoscale shunts under the larger area of Au contacts. However, the dependence of HRS on the contact area is less pronounced than the dependence of LRS. We suggest that this is due to the larger resistivity of $BiFeO_3$ grains at HRS and the RS effect of the irradiated structure is induced mainly by interface-related switching. The switching between HRS and LRS results from the change of Schottky barrier height formed at the interface of metallic contact/perovskite oxide under the voltage.

When V_O generated close to the $BiFeO_3$ surface diffuse through the entire $BiFeO_3$ film at elevated temperature during irradiation or under external electric fields applied during the electrical measurements. V_O are trapped preferentially at defects, e.g., grain boundaries, and thus reduce their resistivity.[21] A conductive "sub-band" may form in the local region of the V_O decorated grain boundaries with high density of gap states.[37] An effective current path can be created. This is demonstrated by the conductive AFM measurements shown in

Figure 4. The current paths serve as conductive shunts in the device structure with top Au electrode.

These shunts are electrically more stable than the defects in the as-grown sample, e.g. randomly distributed V_O, and they contribute as parallel resistance R_S to R_{BFO} (Figure 9a).

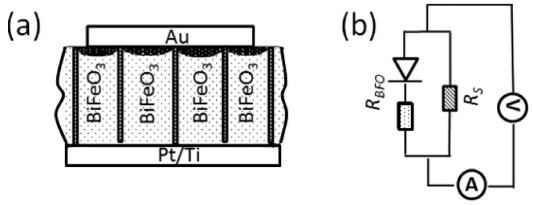

Figure 9. (a) Illustration of irradiation-induced composition and structure change at surface (dark arch pattern) of polycrystalline $BiFeO_3$ and V_O decorated grain boundaries passing through the entire $BiFeO_3$ film (dark stripe pattern). The Schottky contact of Au/$BiFeO_3$ is modified, and these grain boundaries act as conductive paths (shunts) in the irradiated Au/$BiFeO_3$/ Pt memristor. (b) Equivalent schematic diagram. R_S labels the shunt resistance of the conductive paths shown in a.

Therefore, the formation of nanoscale shunts after irradiation enhances the current stability of Au/$BiFeO_3$/ Pt capacitor in the retention measurement. According to Figure 9b, the total resistance R of the Au/irradiated $BiFeO_3$/ Pt structure can be written as

$$\frac{1}{R} = \frac{1}{R_{BFO}} + \frac{1}{R_S} \quad (2)$$

with R_{BFO} described in eq 1.

Note that the formation of stable shunts surrounding the $BiFeO_3$ grains does not play a critical role for the RS effect, which occurs inside the $BiFeO_3$ grains. This is different from the filament formation model for the RS effect.[2] The nanoscale shunts formed in the grain boundaries serve as conductive channel or parallel resistors to the RS unit. This configuration of the circuit may also contribute to the improvement of the current stability.

4. SUMMARY AND OUTLOOK

We have found that oxygen vacancies and metallic Bi phases are controllably created in Ar^+ irradiated $BiFeO_3$ due to preferential sputtering. Therefore, nanoscale shunts are formed and the forming-free resistive switching in the multiferroic $BiFeO_3$ is enhanced. The resistive switching in Au/$BiFeO_3$/Pt structures towards interface-related switching. Ar^+ ion irradiation also modifies the barrier height of the Au/$BiFeO_3$ Schottky contact due to composition and structural changes at the surface of irradiated $BiFeO_3$ films. Trapping of the irradiation-induced oxygen vacancies at defects or grain boundaries facilitates the formation of conductive channels serving as electrically stable shunts. Both the nanoshunt formation and the reduction of the barrier height of the Au/$BiFeO_3$ Schottky contact result in an enhanced current density and significant improvement of the retention stability.

■ ASSOCIATED CONTENT

Ⓢ Supporting Information

TRIDYN (A TRIM simulation code including dynamic composition changes) simulation of the preferential sputtering of the $BiFeO_3$ film and dynamic composition changes under Ar^+ irradiation. This material is available free of charge via the Internet at http://pubs.acs.org.

■ AUTHOR INFORMATION

Corresponding Authors

*E-mail: X.Ou@hzdr.de.
*E-mail: yshuai@uestc.edu.cn.
*E-mail: Heidemarie.Schmidt@etit.tu-chemnitz.de.

Notes

The authors declare no competing financial interest.

■ ACKNOWLEDGMENTS

This work was partially supported by the project Helmholtz-Gemeinschaft Deutscher Forschungszentren under Grant VH-VI-442 and by Deutsche Forschungsgemeinschaft (DFG SCHM1663/4).

■ REFERENCES

(1) Tuller, H. L.; Bishop, S. R. *Annu. Rev. Mater. Res.* **2011**, *41*, 369−398.
(2) Sawa, A. *Mater. Today* **2008**, *11*, 28−36.
(3) Yang, J. J.; Inoue, I. H.; Mikolajick, T.; Hwang, C. S. *MRS Bull.* **2012**, *37*, 131−137.
(4) Cui, Y. M.; Peng, H. Y.; Wu, S. X.; Wang, R. M.; Wu, T. *ACS Appl. Mater. Interfaces* **2013**, *5*, 1213−1237.
(5) Shuai, Y.; Zhou, S.; Bürger, D.; Helm, M.; Schmidt, H. *J. Appl. Phys.* **2011**, *109*, 124117.
(6) Watanabe, Y.; Bednorz, J. G.; Bietsch, A.; Gerber, Ch.; Widmer, D.; Beck, A.; Wind, S. J. *Appl. Phys. Lett.* **2001**, *78*, 3738.
(7) Peng, H.; Wu, T. *Appl. Phys. Lett.* **2009**, *95*, 152106.
(8) Jin, C.; Zheng, D.X.; Li, P.; Mi, W.B.; Bai, H.L. *Appl. Surf. Sci.* **2012**, *263*, 678−681.
(9) Wu, W. T.; Wu, J. J.; Chen, J. S.; Chen, W.-C.; Chen, J.-S. *ACS Appl. Mater. Interfaces* **2013**, *3*, 2616−2621.
(10) Spiga, S.; Lamperti, A.; Wiemer, C.; Perego, M.; Cianci, E.; Tallarida, G.; Lu, H. L.; Alia, M.; Volpe, F. G.; Fanciulli, M. *Microelectron. Eng.* **2008**, *85*, 2414−2419.
(11) Walczyk, Ch.; Wenger, Ch.; Sohal, R.; Lukosius, M.; Fox, A.; Dabrowski, J.; Wolansky, D.; Tillack, B.; Müssig, H.-J.; Schroeder, T. *J. Appl. Phys.* **2009**, *105*, 114103.
(12) Reagor, D. W.; Butko, V. Y. *Nat. Mater.* **2005**, *4*, 593−596.
(13) Rodenbücher, C.; Wicklein, S.; Waser, R.; Szot, K. *Appl. Phys. Lett.* **2013**, *102*, 101603.
(14) Heiko, G.; Seongshik, O. *Appl. Phys. Lett.* **2011**, *99*, 092105.
(15) Kan, D.; Terashima, T.; Kanda, R.; Masuno, A.; Tanaka, K.; Chu, S.; Kan, H.; Ishizumi, A.; Kanemitsu, Y.; Shimakawa, Y.; Takano, M. *Nat. Mater.* **2005**, *4*, 816−819.
(16) Ngai, J. H.; Segal, Y.; Walker, F. J.; Ahn, C. H. *Phys. Rev. B* **2011**, *83*, 045304.
(17) Bruno, F. Y.; Tornos, J.; Gutierrez del Olmo, M.; Sanchez Santolino, G.; Nemes, N. M.; Garcia-Hernandez, M.; Mendez, B.; Piqueras, J.; Antorrena, G.; Morellon, L.; De Teresa, J. M.; Clement, M.; Iborra, E.; Leon, C.; Santamaria, J. *Phys. Rev. B* **2011**, *83*, 245120.
(18) Wang, J.; Neaton, J. B.; Zheng, H.; Nagarajan, V.; Ogale, S. B.; Liu, B.; Viehland, D.; Vaithyanathan, V.; Schlom, D. G.; Waghmare, U. V.; Spaldin, N. A.; Rabe, K. M.; Wuttig, M.; Ramesh, R. *Science* **2003**, *299*, 1719−1722.
(19) Yang, C. H.; Seidel, J.; Kim, S. Y.; Rossen, P. B.; Yu, P.; Gajek, M.; Chu, Y. H.; Martin, L.W.; Holcomb, M. B.; He, Q.; Maksymovych, P.; Balke, N.; Kalinin, S. V.; Baddorf, A. P.; Basu, S. R.; Scullin, M. L.; Ramesh, R. *Nat. Mater.* **2009**, *8*, 485−493.
(20) Luo, J. M.; Lin, S. P.; Zheng, Y.; Wang, B. *Appl. Phys. Lett.* **2012**, *101*, 062902.
(21) Yin, K.; Li, M.; Liu, Y.; He, C.; Zhuge, F.; Chen, B.; Lu, W.; Pan, X.; Li, R.W. *Appl. Phys. Lett.* **2010**, *97*, 042101.

(22) Jiang, A. Q.; Wang, C.; Jin, K. J.; Liu, X. B.; Scott, J. F.; Hwang, C. S.; Tang, T. A.; Lu, H. B.; Yang, G. Z. *Adv. Mater.* **2011**, *23*, 1277−1281.
(23) Tsurumaki, A.; Yamada, H.; Sawa, A. *Adv. Funct. Mater.* **2012**, *22*, 1040−1047.
(24) Xu, Q. Y.; Yuan, X. Y.; Cao, Y. Q.; Si, L. F.; Wu, D. *Solid State Commun.* **2012**, *152*, 2036−2039.
(25) Wang, S. Y.; Tseng, T. Y. *J. Adv. Dielectr.* **2011**, *1*, 141−162.
(26) Cui, Y.; Tian, Y. F.; Liu, W.; Li, Y. F.; Wang, R. M.; Wu, T. *AIP Adv.* **2011**, *1*, 042129.
(27) Muenstermann, R.; Menke, T.; Dittmann, R.; Waser, R. *Adv. Mater.* **2010**, *22*, 4819−4822.
(28) Mayr, C.; Stärke, P.; Partzsch, J.; Cederstroem, L.; Schüffny, R.; Shuai, Y.; Du, N.; Schmidt, H. *Proc. NIPS* **2012**, 1709−1717.
(29) Möller, W.; Eckstein, W. *Nucl. Instrum. Methods Phys. Res., Sect. B* **1984**, *2*, 814−818.
(30) Gross, H.; Bansal, N.; Kim, Y.-S.; Oh, S. *J. Appl. Phys.* **2011**, *110*, 073704.
(31) Toma, A.; Setina Batic, B.; Chiappe, D.; Boragno, C.; Valbusa, U.; Godec, M.; Jenko, M.; Buatier de Mongeot, F. *J. Appl. Phys.* **2008**, *104*, 104313.
(32) Luo, W.B.; Zhu, J.; Li, Y. R.; Wang, X. P.; Zhao, D.; Xiong, J.; Zhang, Y. *Appl. Phys. Lett.* **2007**, *91*, 082501.
(33) Asami, K.; Koiwa, I.; Yamanobe, T. *Jpn. J. Appl. Phys.* **1999**, *38*, 5423−5427.
(34) Béa, H.; Bibes, M.; Barthélémy, A.; Bouzehouane, K.; Jacquet, E.; Khodan, A.; AContour, J. -P.; Fusil, S.; Wyczisk, F.; Forget, A.; Lebeugle, D.; Colson, D.; Viret, M. *Appl. Phys. Lett.* **2005**, *87*, 072508.
(35) Shuai, Y.; Ou, X.; Luo, W.; Du, N.; Wu, C.; Zhang, W.; Bürger, D.; Mayr, C.; Schüffny, R.; Zhou, S.; Helm, M.; Schmidt, H. *IEEE Electron Device Lett.* **2012**, *34*, 54−56.
(36) Shuai, Y.; Ou, X.; Luo, W.; Mucklich, A.; Burger, D.; Zhou, S.; Wu, C.; Chen, Y.; Zhang, W.; Helm, M.; Mikolajick, T.; Schmidt, O.G.; Schmidt, H. *Sci. Rep.* **2013**, *3*, 2208.
(37) Bersuker, G.; Gilmer, D. C.; Veksler, D.; Yum, J.; Park, H.; Lian, S.; Vandelli, L.; Padovani, A.; Larcher, L.; McKenna, K.; Shluger, A.; Iglesias, V.; Porti, M.; Nafría, M.; Taylor, W.; Kirsch, P. D.; Jammy, R. *IEDM Tech. Dig.* **2010**, 456−459.